JBC RESEARCH ARTICLE

The two paralogous copies of the YoeB–YefM toxin–antitoxin module in *Staphylococcus aureus* differ in DNA binding and recognition patterns

Received for publication, September 11, 2021, and in revised form, November 24, 2021 Published, Papers in Press, November 30, 2021,
https://doi.org/10.1016/j.jbc.2021.101457

Lu Xue[1,2,‡], **Muhammad Hidayatullah Khan**[1,2,‡], **Jian Yue**[1,2], **Zhongliang Zhu**[1,2,*], **and Liwen Niu**[1,2,*]

From the [1]*Hefei National Laboratory for Physical Sciences at the Microscale, Division of Molecular and Cellular Biophysics, and* [2]*Division of Life Sciences and Medicine, School of Life Sciences, University of Science and Technology of China, Hefei, Anhui, China*

Edited by Chris Whitfield

Toxin–antitoxin (TA) systems are ubiquitous regulatory modules for bacterial growth and cell survival following stress. YefM–YoeB, the most prevalent type II TA system, is present in a variety of bacterial species. In *Staphylococcus aureus*, the YefM–YoeB system exists as two independent paralogous copies. Our previous research resolved crystal structures of the two oligomeric states (heterotetramer and heterohexamer–DNA ternary complex) of the first paralog as well as the molecular mechanism of transcriptional autoregulation of this module. However, structural details reflecting molecular diversity in both paralogs have been relatively unexplored. To understand the molecular mechanism of how Sa_2YoeB and Sa_2YefM regulate their own transcription and how each paralog functions independently, we solved a series of crystal structures of the Sa_2YoeB–Sa_2YefM. Our structural and biochemical data demonstrated that both paralogous copies adopt similar mechanisms of transcriptional autoregulation. In addition, structural analysis suggested that molecular diversity between the two paralogs might be reflected in the interaction profile of YefM and YoeB and the recognition pattern of promoter DNA by YefM. Interaction analysis revealed unique conformational and activating force effected by the interface between Sa_2YoeB and Sa_2YefM. In addition, the recognition pattern analysis demonstrated that residues Thr^7 and Tyr^{14} of Sa_2YefM specifically recognizes the flanking sequences (G and C) of the promoter DNA. Together, these results provide the structural insights into the molecular diversity and independent function of the paralogous copies of the YoeB–YefM TA system.

Toxin–antitoxin (TA) systems form fascinating small regulatory networks that regulate different aspects of microbial physiology including bacterial growth and survival during stress conditions. These systems are comprised of stable growth-inhibiting toxin and labile neutralizing antitoxin. They are found on the low copy number plasmids, bacterial chromosome, and bacteriophage (1–3). TA systems are classified into six different classes (I–VI) on the basis of their biochemical nature and neutralizing mechanism of antitoxins (4–6). Type II TA systems are well-characterized modules consisting of stable toxin and labile antitoxin canonically positioned adjacently within the same operon. Under normal growth condition, labile antitoxin inhibits the activity of toxin by forming tight nontoxic TA complex. However, in response to stress, antitoxins are selectively degraded by cellular proteases, followed by the release of free toxin from their corresponding antitoxin that might result in the cell growth arrest or cell death. Toxins acts as intracellular "molecular time bombs" that could regulate various essential biocellular processes, that is, gene expression at transcriptional and post-transcriptional levels by mRNA decay (7). Most type II toxins (RelE, YoeB, and YafQ) exhibit RNase activity that inhibits translation by cleaving mRNA (8–10).

Classic type II antitoxins are small proteins that serve as a substrate for several host proteases such as Lon and ClpP (11). These proteins are comprised of two distant and functional domains, that is, N-terminal domain for binding promoter DNA to regulate transcription of TA operon and C-terminal domain responsible for binding the cognate toxin to neutralize its activity. Majority of the bacterial type II TA operons are autoregulated by antitoxin, serving as a repressor and toxin as a corepressor that result in the increase of transcriptional repression (12, 13). However, some type II TA operons (*relBE*, *ccdAB*, and *phd/doc*) are regulated by a complex mechanism termed as "conditional cooperativity," which allow low/high concentration of toxin to act as a corepressor/depressor that could stimulate/disrupt binding of antitoxin to the promoter DNA, respectively (5, 14–16). Conditional cooperativity in these type II TA systems can be conferred by different molar ratio of toxin to antitoxin, protein dynamics, DNA-binding affinity, and intrinsic disordered region in the C terminus of antitoxin without the cognate toxin binding (17).

The chromosomal *yefm/yoeb* system (also known as axe/txe), one of the type II TA systems, is mostly found in many bacterial species including major pathogens, that is, *Streptococcus pneumoniae*, *Mycobacterium tuberculosis*, *Streptococcus suis*, and *Staphylococcus aureus* (18–21). YefM antitoxin could inhibit the RNase activity of YoeB by forming

‡ These authors contributed equally to this work.
* For correspondence: Zhongliang Zhu, zlzhu63@ustc.edu.cn; Liwen Niu, lwniu@ustc.edu.cn.

a tight YoeB–YefM complex (22). Overproduction of the Lon protease specifically activates YoeB-dependent mRNA cleavage by degrading YefM (23). The released YoeB could bind the 70S ribosome and cleaves mRNA at the second position of A site codon that results in inhibiting translation initiation (9, 24).

In *S. aureus*, two independent paralogous copies of chromosomally encoded YoeB–YefM TA loci (Sa_1YoeB–Sa_1YefM and Sa_2YoeB–Sa_2YefM) can be found simultaneously in the same strain (25–27). Both paralogous toxins share 30% sequence identity and 45% similarity. Similarly, both antitoxins exhibit 25% sequence identity and 47% similarity. Despite the high sequence similarity, both YoeB–YefM paralogous systems are functionally independent of each other. For instance, antitoxin from each paralog could only neutralize its own toxin, and each system is transcriptionally autoregulated by their own cognate antitoxin and toxin (21, 26). Our previous work demonstrated that the Sa_1YoeB–Sa_1YefM complex exists as two different oligomeric states, which exhibit distinct promoter DNA–binding affinity. Based on the crystal structures and corresponding biochemical experiments, molecular mechanism for the transcriptional autoregulation *via* conditional cooperativity was proposed (28). However, the in-depth structural details corresponding the molecular diversity in the two paralogous copies have been relatively unexplored. Here, we set out to understand the molecular mechanism how Sa_2YoeB–Sa_2YefM regulates its own transcription and how each paralog function independently?

In the present study, we determined the crystal structures of heterohexamer (Sa_2YoeB_2–Sa_2YefM_4), heterotetramer (Sa_2YoeB_2–Sa_2YefM_2), and heterohexamer–DNA ternary complex (Sa_2YoeB_2–Sa_2YefM_4–DNA), followed by biochemical analysis. These structures highlight the mechanistic conformational changes in the C terminus as well as the central helices of Sa_2YefM upon binding of Sa_2YoeB, which could be responsible for the stability of diverse oligomeric states. Both YoeB–YefM paralogs adopt similar mechanism to regulate their own transcription. For instance, hydrogen bond network between the two heterotrimers is critical for the heterohexameric state formation and optimal DNA-binding affinity. In contrast, the steric clashes because of the simultaneous binding of two heterotetramers to the adjacent promoter DNA sites disrupt DNA-binding affinity. Molecular diversity in the two paralogs was investigated by comparative analysis of interaction profile of YefM and YoeB and recognition pattern of YefM and DNA. First, the conformation and acting force of interface between toxin and antitoxin are unique for Sa_2YoeB–Sa_2YefM. Second, Sa_2YefM could recognize the flanking nucleotide sequences "G" and "C" by residues Thr^7 and Tyr^{14}, whereas Sa_1YefM could recognize the flanking nucleotide "T" by residues Tyr^6 and Ser^7. Together, these results suggested that both YoeB–YefM paralogs could function independently. The outcome of the current study will provide an in-depth understanding about the structural biology of the two paralogous copies of YefM–YoeB in *S. aureus* and will facilitate researchers to develop antimicrobial strategies.

Results

Structures of two oligomeric states of Sa_2*YoeB–*Sa_2*YefM*

Consistent with the Sa_1YoeB–Sa_1YefM states (28), size-exclusion chromatography coupled with multilight angle scattering (SEC-MALS) experiments reflected that Sa_2YoeB–Sa_2YefM also exhibit various oligomeric states in solution. The purified Sa_2YoeB–Sa_2YefM complex in solution depicted molecular weight of about 56 kDa (Fig. S1), corresponding the stoichiometry of heterohexamer state. In heterohexamer (Sa_2YoeB_2–Sa_2YefM_4) structure, each Sa_2YefM dimer is linked with the Sa_2YoeB monomer, and two Sa_2YoeB molecules are spatially separated by two dimeric Sa_2YefM molecules. The C-terminal regions of each dimeric Sa_2YefM molecule adopt two different conformations, that is, one dimer is structurally ordered because of binding of globular YoeB monomer, whereas the other dimer is structurally disordered (Fig. 1*A*). Superposition of heterohexamer structures from the two paralogs demonstrated that the structure of Sa_2YoeB_2–Sa_2YefM_4 is similar to the structure of Sa_1YoeB_2–Sa_1YefM_4–DNA (RMSD of 1.96 Å; Fig. S2*A*).

Heterotetramer (Sa_2YoeB_2–Sa_2YefM_2) complex was obtained by denaturing and refolding method. SEC–MALS analysis depicted molecular weight of the protein complex as ∼36 kDa, which is consistent with the theoretical molecular weight of the heterotetramer (∼40 kDa), as illustrated in Fig. S1. To further determine the diverse nature of Sa_2YoeB–Sa_2YefM, we solved the crystal structure of heterotetramer in which dimeric Sa_2YefM molecule bridges the two Sa_2YoeB molecules spatially separated by the dimeric Sa_2YefM molecules (Fig. 1*B*). In comparison with the heterohexamer structure, all the C-terminal segments of Sa_2YefM molecules are well structured upon binding the Sa_2YoeB molecules. Superposition of the paralogous heterotetramer structures revealed that Sa_2YoeB_2–Sa_2YefM_2 heterotetramer is consistent with Sa_1YoeB_2–Sa_1YefM_2 heterotetramer (RMSD of 2.44 Å; Fig. S2*B*).

Conformational transition of Sa_2*YefM within two oligomeric states*

Because of the absence of Sa_1YoeB_2–Sa_1YefM_4 heterohexamer structure in *apo*-form, the molecular mechanism of conformational transition of YefM in the two oligomeric states still remains elusive. Comparative analysis of Sa_2YefM dimer in the structures of heterohexamer and heterotetramer demonstrated similar folds with the exception in different conformation of the third set of helices and the C-terminal region (Fig. 2*A*). In the structure of heterohexamer, the third set of α-helices of Sa_2YefM homodimer with different lengths (H3: Leu43–Ile53 and $H3^{\#}$: $Leu43^{\#}$–$Thr58^{\#}$) connecting N-terminal domain to the C-terminal region crosses at an angle of about 63°. The remaining residues (Tyr54–Leu85) of one Sa_2YefM molecule are involved in the formation of C-terminal disorder region, whereas residues ($Gly59^{\#}$–$Leu85^{\#}$) of another Sa_2YefM molecule are mainly associated with the formation of three secondary structural elements including helix $H4^{\#}$ ($Thr60^{\#}$–$Lys69^{\#}$), β sheet $S3^{\#}$ ($Thr74^{\#}$–$Asn76^{\#}$), and

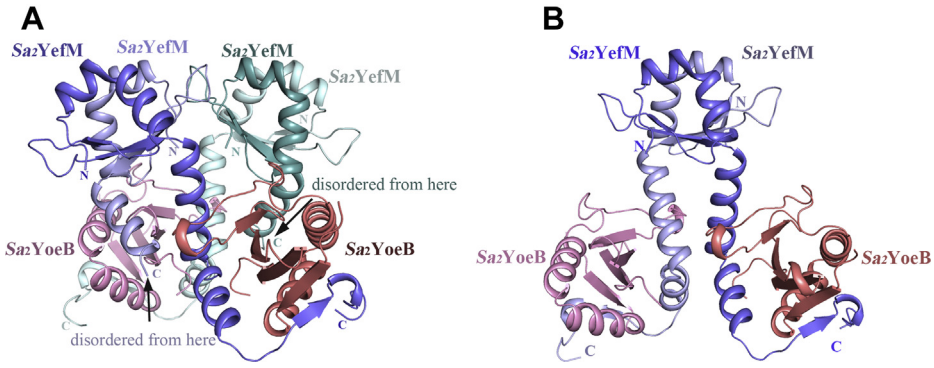

Figure 1. Structures of heterotetramer and heterohexamer complex. *A*, overall structure of heterohexamer (Sa_2YoeB–Sa_2YefM$_2$–Sa_2YefM$_2$–Sa_2YoeB) complex. Two intact Sa_2YefM molecules are shown in *slate/pale cyan*, whereas other two Sa_2YefM molecules with disordered C terminus are shown in *light blue/deep teal*. Two Sa_2YoeB molecules are indicated in *pink/salmon*. *B*, overall structure of the heterotetramer (Sa_2YoeB–Sa_2YefM$_2$–Sa_2YoeB) complex is illustrated in *cartoon*, Sa_2YefM is shown in *salmon* and *light blue*, whereas Sa_2YoeB is shown in *pink* and *salmon*.

helix H5$^{\#}$ (Asn76$^{\#}$–Asp79$^{\#}$) as depicted in Figure 2*B*. In contrast, the H3 helix in Sa_2YoeB$_2$–Sa_2YefM$_2$ heterotetramer (Sa_2YefM$^{Leu43–Thr58}$) is slightly longer than Sa_2YoeB$_2$–Sa_2YefM$_4$ heterohexamer (Sa_2YefM$^{Leu43–Ile53}$). The remaining residues adopt similar folding as Sa_2YefM$^{Gly59\#–Leu85\#}$, and the crossing angle (∼54°) of H3 and H3$^{\#}$ is smaller than heterohexamer (Fig. 2*C*).

Comparison of Sa_2YefM structures within the two different oligomeric complexes highlights the mechanistic conformational changes in the C-terminal and central helices (H3 and H3$^{\#}$) of Sa_2YefM. The first conformational change is essential for the formation of heterohexamer. The C-terminal region of all Sa_2YefM molecules in the hypothetical heterohexamer are well structured, and the steric collision of the hypothetical helices (H4$^{\#}$ and H4) might destroy the stable conformation of heterohexamer (Fig. 3*A*). Different angles of the two central helices (H3 and H3$^{\#}$) are essential for the formation of different oligomers. For instance, the two central helices (H3 and H3$^{\#}$) in the theoretical heterotetramer adopt an angle of 63°, and the helices H4 and H4$^{\#}$ would be sterically hindered (Fig. 3*A*). In contrast, the two central helices in the theoretical heterohexamer adopt an angle of 54°, which would be resolved by clash in the interface of heterotrimer (Fig. 3*B*). Collectively, these results concluded that the mechanistic conformational

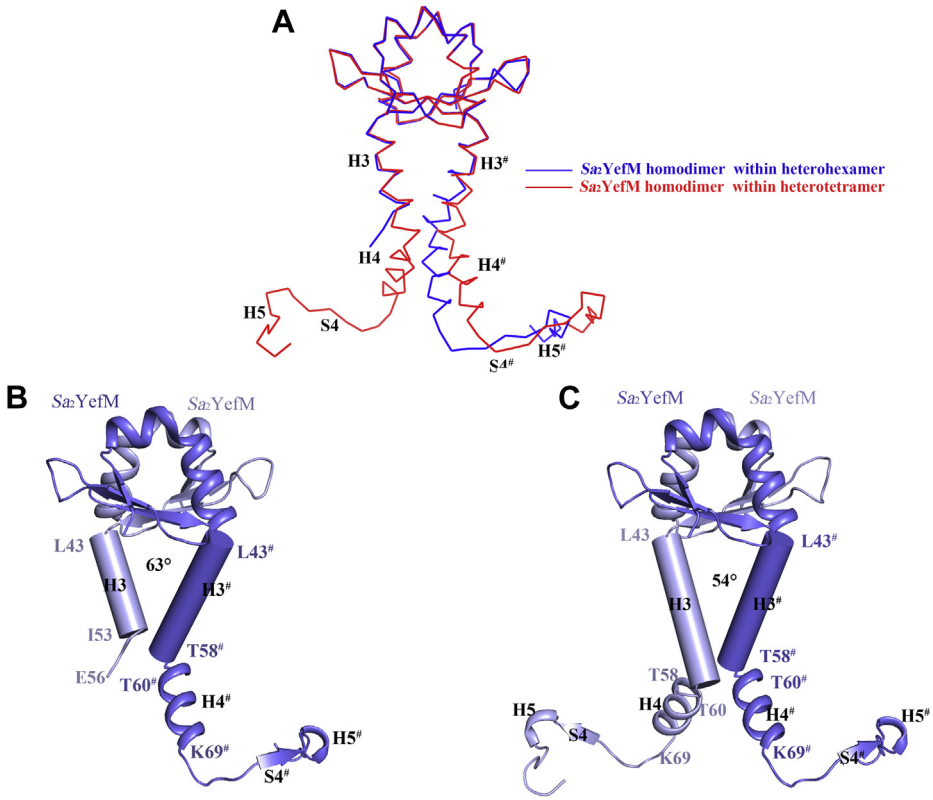

Figure 2. Conformational transition of Sa_2YefM within two oligomeric states. *A*, superposition of the structures of Sa_2YefM homodimer within heterohexamer (*blue*) and heterotetramer (*red*). Structure of Sa2YefM homodimer within (*B*) heterohexamer and (*C*) heterotetramer.

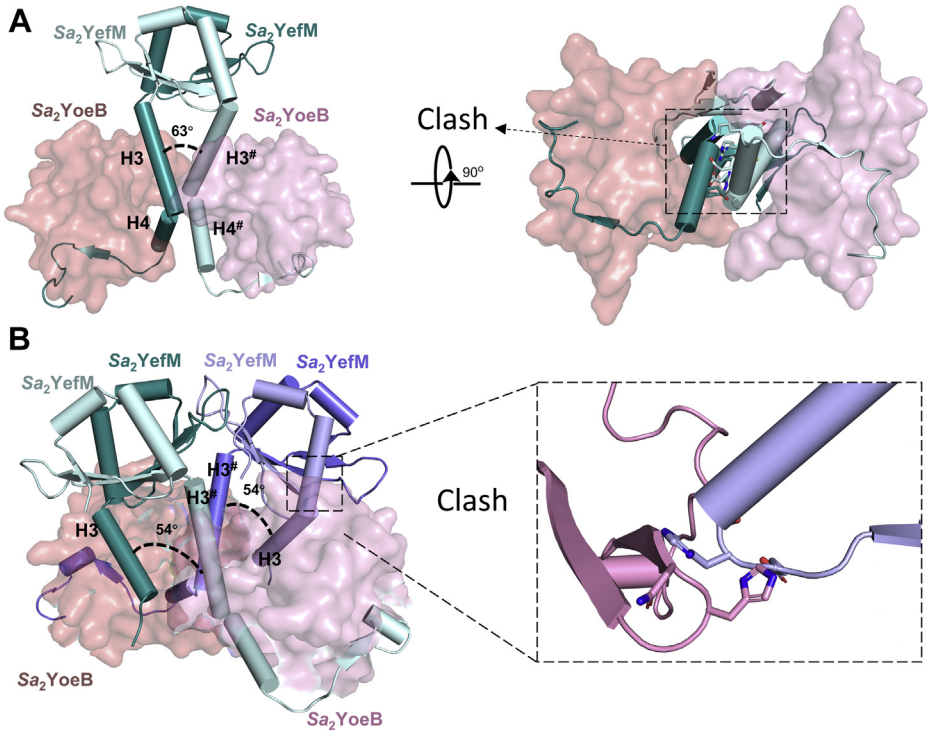

Figure 3. Steric clashes in the theoretical heterotetramer and heterohexamer because of the conformation changes in the C terminus and central helices (H3 and H3$^{\#}$) of *Sa*$_2$YefM, resulting in the unstable conformation of the corresponding complex. *A*, steric collision in the hypothetical helices (H4 and H4$^{\#}$) of the theoretical heterotetramer at the crossing angle between central helices (H3 and H3$^{\#}$) as 63°. *Right panel* presents the clash observed from the inverted side of the interface. *B*, steric clashes in the two heterotrimers because of the crossing angle (54°) in the central H3 and H3$^{\#}$ helices of the theoretical heterohexamer. *Right panel* reflects the close-up view of the steric clashes in heterotrimers.

changes in the C-terminal region and central helices of Sa_2YefM upon Sa_2YoeB binding might be a strategy to stabilize the diverse oligomeric complexes.

Two YoeB–YefM paralogs adopt similar mechanism of regulation

Consistent with the Sa_1YoeB–Sa_1YefM (28), biochemical experiments including EMSA and isothermal titration calorimetry (ITC) reflected that heterohexamer (Sa_2YoeB$_2$–Sa_2YefM$_4$) exhibits higher promoter DNA–binding affinity as compared with heterotetramer (Sa_2YoeB$_2$–Sa_2YefM$_2$) and Sa_2YefM alone (Fig. S3 and Table S4). Analysis of heterohexamer structure revealed that heterohexamers (Sa_2YefM$_4$–Sa_2YoeB$_2$) are mainly composed of two heterotrimers (Sa_2YefM$_2$–Sa_2YoeB) linked together by hydrogen bonds. The hydrogen bond networks are mainly associated with residues (Gln44, Ser45, Arg60, Ile61, and His63) of Sa_2YoeB molecule of one heterotrimer and residues (Asn23, His24, Asp45, and Ser48) of Sa_2YefM molecule of another heterotrimer (Fig. S4*A*). Similar hydrogen bond networks were also found in the crystal structure of Sa_1YefM–Sa_1YoeB heterohexamer (28). To more systematically assess the role of hydrogen bond network in the formation of heterohexamer, we substituted six residues (Sa_2YefM^{Asn23Ala}, Sa_2YefM^{Asp45Ala}, Sa_2YefM^{Ser48Ala}, Sa_2YoeB^{Ser45Ala}, Sa_2YoeB^{Arg60Ala}, and Sa_2YoeB^{His63Ala}). The corresponding experiments such as SEC–MALS, EMSA, and ITC revealed that the mutant complex exists as heterotrimer and possesses weaker DNA-binding affinity as compared with heterohexamer (Fig. S4, *B–D*). These results demonstrated that the hydrogen bond network is critical for the heterohexameric state and optimal DNA-binding affinity.

To understand why the heterohexamer possesses higher DNA-binding affinity than the heterotetramer, we determined the crystal structure of heterohexamer (Sa_2YefM$_4$–Sa_2YoeB$_2$) in complex with 26 bp promoter DNA. There are two adjacent binding sites on the promoter DNA for two Sa_2YefM dimers of heterohexamer. Theoretically, single promoter DNA should bind two heterotetramers; however, the simultaneous binding of two heterotetramers to the adjacent sites on the single promoter would sterically clash with each other, resulting in the release of heterotetramers and subsequently open the way for transcription (Fig. S5). This steric exclusion is also found in two Sa_1YoeB$_2$–Sa_1YefM$_2$ heterotetramers (28). Hence, we concluded that the two YoeB–YefM paralogs adopt similar mechanism to regulate their transcription.

Unique interaction of Sa$_2$*YoeB and* Sa$_2$*YefM*

Previous research demonstrated that the two paralogs (Sa_1YefM–Sa_1YoeB and Sa_2YefM–Sa_2YoeB) do not cross talk with each other (26), although they share higher sequence similarity and exhibit similar mechanism for their transcriptional autoregulation. To more systematically assess the molecular diversity in the two YoeB–YefM paralogs, unique aspects of the interface of Sa$_2$YefM–Sa$_2$YoeB complex were analyzed. The contact interface between Sa_2YefM and Sa_2YoeB is ∼1610 Å^2, and about 26% of the surface of

Sa_2YoeB is buried upon interaction with the corresponding Sa_2YefM. The $Sa_2YefM^{Leu43–Leu85}$ comprised of three helices (H3, H4, and H5) and one sheet (S3), surrounding the toxin Sa_2YoeB by forming an arm, is sufficient to protect against Sa_2YoeB *via* two faces (Fig. 4*A*). In one interface (interface 1), the $Sa_2YefM^{Leu43–Asp70}$ binds into a groove of Sa_2YoeB of which four-stranded β sheets (β1, β2, β3, and β4) form the base and is flanked by α1-helix on one side and α3-helix on the other side, followed by the formation of L-shaped turn consisting of two helices (H3 and H4). Specifically, the H3 helix of Sa_2YefM mainly interacts with Sa_2YoeB *via* hydrogen bonds (Sa_2YefM^{Glu51}–Sa_2YoeB^{Arg66}, Sa_2YefM^{Glu51}–Sa_2YoeB^{Ser58}, and Sa_2YefM^{Tyr54}–Sa_2YoeB^{Gln64}) and a pair of electrostatic interaction (Sa_2YefM^{Glu51}–Sa_2YoeB^{Arg66}). The H4 helix primarily interacts with Sa_2YoeB *via* four pairs of electrostatic interaction (Sa_2YefM^{Lys63}–Sa_2YoeB^{Asp15}, Sa_2YefM^{Arg67}–Sa_2YoeB^{Asp15}, Sa_2YefM^{Glu68}–Sa_2YoeB^{Arg56}, and Sa_2YefM^{Asp70}–Sa_2YoeB^{Lys9}) and a pair of hydrogen bond (Sa_2YefM^{Asp70}–Sa_2YoeB^{Ser11}) (Fig. 4*B*). In addition, some hydrophobic interactions formed by the small aliphatic side chains of Sa_2YefM (Leu55, Met61, and Val64) and Sa_2YoeB (Leu49, Val68, and Leu81) also support this interface (Fig. 4*C*). In the other interface (interface 2), the $Sa_2YefM^{Asn71–Leu85}$ extends to the dorsal side of Sa_2YoeB created by three N-terminal secondary structural elements (β1, α1, and α2) and adopts an extended β strand (S4) and short helix (H4) with extensive contacts. Specifically, hydrogen bond networks are mainly supported by the residues ($Sa_2YefM^{Asn71–Asn76}$ and $Sa_2YoeB^{Val6–Ser11}$). Hydrophobic interactions are associated with the side chain of hydrophobic residues of Sa_2YefM (Ile77, Ile80, and Trp88) inserted into the hydrophobic groove of Sa_2YoeB provided by the hydrophobic residues (Val6, Ile8, Leu16, Ile19, Phe28, Leu29, Val32, and Leu35). The acidic residue (Asp78) of $YefM^{Leu77–Leu85}$ neutralizes the basic residue (Lys36) of Sa_2YoeB *via* electrostatic interaction (Fig. 4*D*).

Comparison of tertiary structures demonstrated obvious structural differences of TA interface in the two YefM–YoeB paralogs (Fig. 5). In interface 1, Sa_2YefM adopts larger angle of L-turn and shorter H4 helix length as compared with Sa_1YefM. The helix (α3) of Sa_2YoeB orientates away from the L-turn of Sa_2YefM; however, the same region in Sa_1YoeB lies toward the L-turn of their cognate antitoxin. Residue Sa_1YoeB^{Leu56} involved in the hydrophobic interaction with the L-turn of YefM is replaced by Sa_2YoeB^{Tyr53}, resulting in the difference in the orientation of α3-helix. In interface 2, Sa_2YefM could form a moderate-length β-sheet and a small α-helix at the hydrophobic groove of the corresponding toxins, whereas Sa_1YefM can form a long β-sheet. In addition, TA interface in Sa_2YefM–Sa_2YoeB presents more pairs of electrostatic interaction as compared with Sa_1YefM–Sa_1YoeB. These analyses reflected that the interactions between Sa_2YefM and Sa_2YoeB are unique for Sa_2YoeB–Sa_2YefM TA system. Together, different interaction patterns of the two YefM–YoeB paralogs could explain why YefM

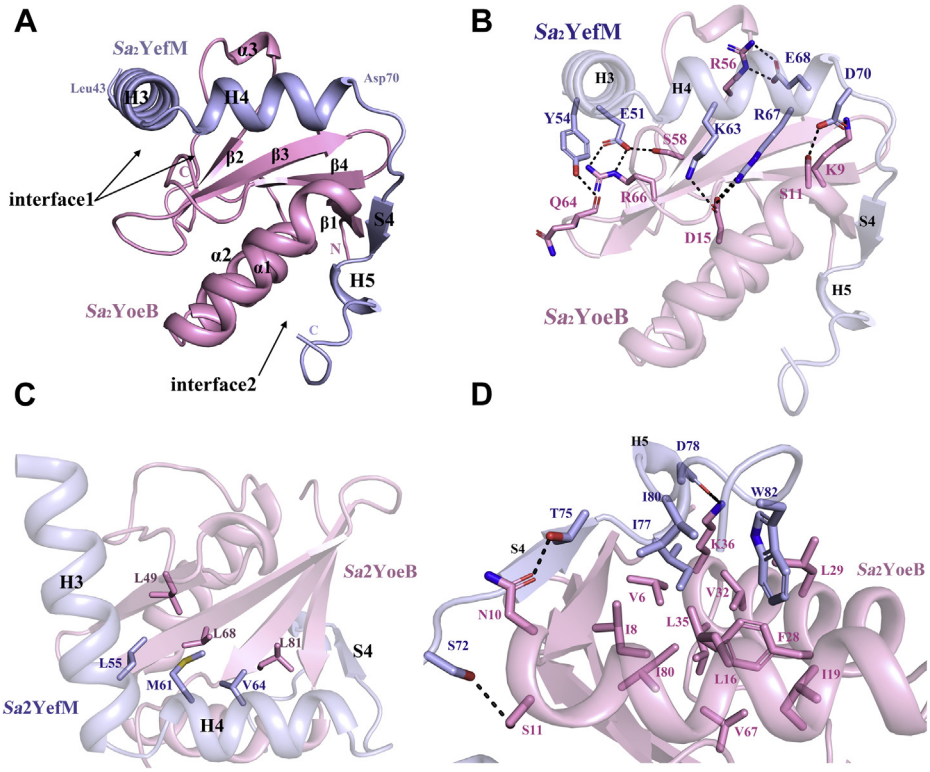

Figure 4. Interactions between Sa_2YoeB and Sa_2YefM. *A*, the two interfaces between Sa_2YoeB and Sa_2YefM. *B*, hydrogen bonds and electrostatic interaction in the interface 1. *C*, hydrophobic interactions in interface 1. *D*, hydrogen bonds, hydrophobic interactions, and electrostatic interactions in interface 2. Residues of Sa_2YoeB (*pink*) and Sa_2YefM (*light blue*) are shown as *sticks*. The detailed hydrogen bonds and electrostatic interaction of Sa_2YoeB and Sa_2YefM are presented as *black dashed lines*.

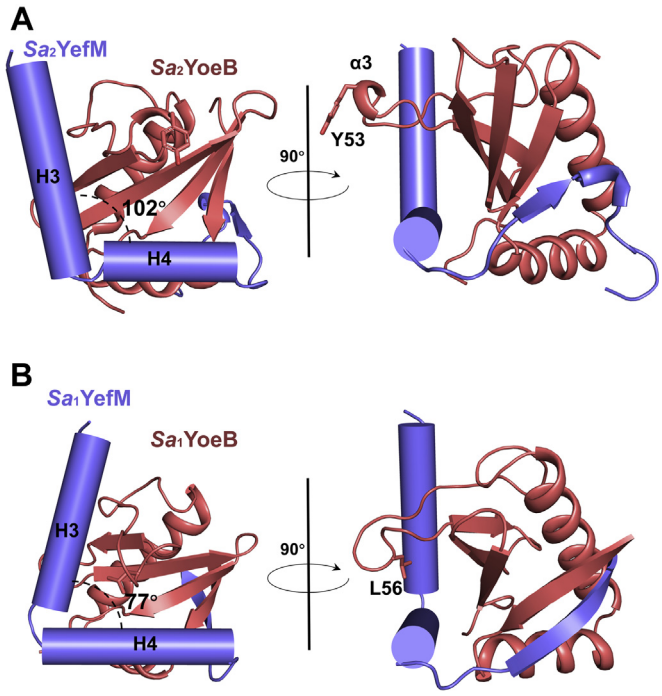

Figure 5. The conformation of interface between YoeB toxin and YefM antitoxin. The conformation of interface between (*A*) Sa_2YoeB (*salmon*) and Sa_2YefM (*blue*) and (*B*) Sa_1YoeB (*salmon*) and Sa_1YefM (*blue*). *Right panels* present the conformation of interface from the inverted view.

from one system cannot abolish toxicity of YoeB from another system.

Unique recognition pattern of Sa_2*YefM and DNA*

To further explore the diversity in the two paralogs, molecular interactions of Sa_2YefM antitoxin with the promoter DNA were analyzed. Each Sa_2YefM dimer within heterohexamer contacts the duplex DNA *via* N-terminal DNA-binding domain composed of winged helix–turn–helix (HTH) motif. The N-terminal helices (H1 and H2) of Sa_2YefM dimer form large positively charged surface that locks into the major groove of DNA, with the β-hairpin wing connecting strands (S2 and S3) inserted into the adjacent minor groove (Fig. 6). The sequence of Sa_2YefM–Sa_2YoeB promoter DNA is comprised of adjacent long and short palindromes with core 5′-GTAC-3′ motifs with a center-to-center distance of 11 bp (Fig. 7*A*). The specific recognition of core palindromic quadruplet "GTAC" in the two palindromes (G_6:$C_{21'}$ to C_9:$G_{18'}$ and G_{16}:$G_{11'}$ to C_{23}:$G_{4'}$) is primarily achieved by hydrogen bonds between the bases (guanine and thymidine) and arginine residue (Arg^{10}) in H1 helix of Sa_2YefM dimer (Fig. 7, *A* and *B*). The terminal Nη1 and Nη2 groups of Arg^{10}(A)/Arg^{10}(B)/Arg^{10}(C)/Arg^{10}(D) donate hydrogen bonds to the O6 and N7 atoms of $G_{18'}$/G_6/G_{18}/$G_{6'}$ in a bifurcated hydrogen-bonding pattern. In addition, the Nη1 group of Arg^{10}(A)/Arg^{10}(C) interacts with the O4 atom of $T_{19'}$/T_{19} *via* single hydrogen bond. These hydrogen bondings confer the specific recognition of GTAC quadruplet. To investigate whether GTAC quadruplet affects the interaction, nucleotide sequences G:C (G_6, C_9, C_{18}, G_{21}) and T:A (T_7, A_8, A_{19}, T_{20}) in the core sequences were mutated to T:A and G:C pairs, respectively. Results reflected that mutation in the core promoter DNA sequence could abolish the interaction of heterohexamer with the promoter DNA (Fig. S6*A*), suggesting the critical role of the core sequence in the recognition and binding pattern. The recognition patterns for guanine–arginine and thymidine–arginine are consistent with Sa_1YefM–Sa_1YoeB (28).

Our previous work demonstrated that the flanking sequence is also critical for the specific recognition (28). Sequence alignment of promoter for both paralogs (Fig. S6*C*) depicted significant difference in the flanking sequence, which could specifically interact with the H1 and H2 helices of Sa_2YefM. Most obvious feature of helix H2 of Sa_2YefM is the van der Waals (VDW) packing of an aromatic residue (Tyr^{14}) against bases in the major groove. Specifically, the aromatic ring of

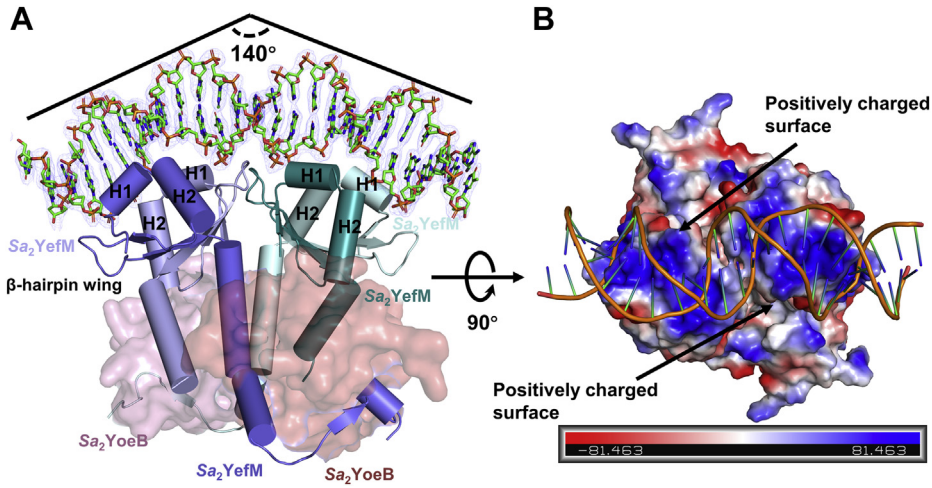

Figure 6. Structure of heterohexamer–DNA complex. *A*, overall structure of the heterohexamer–DNA (Sa_2YoeB–Sa_2YefM$_2$–Sa_2YefM$_2$–Sa_2YoeB–DNA) complex is illustrated in *cartoon*. DNA molecule attached to the heterohexamer bends at an angle of 40°. Two intact Sa_2YefM molecules are shown in *slate/pale cyan*, whereas other two Sa_2YefM molecules with disordered C terminus are shown in *light blue/deep teal*. Two Sa_2YoeB molecules are illustrated by *pink/salmon*. The $2F_o$–F_c electron density map is displayed at the level of 1.0σ around the DNA molecule. *B*, orientation of heterohexamer–DNA (Sa_2YoeB–Sa_2YefM$_2$–Sa_2YefM$_2$–Sa_2YoeB–DNA) complex rotated by 90°.

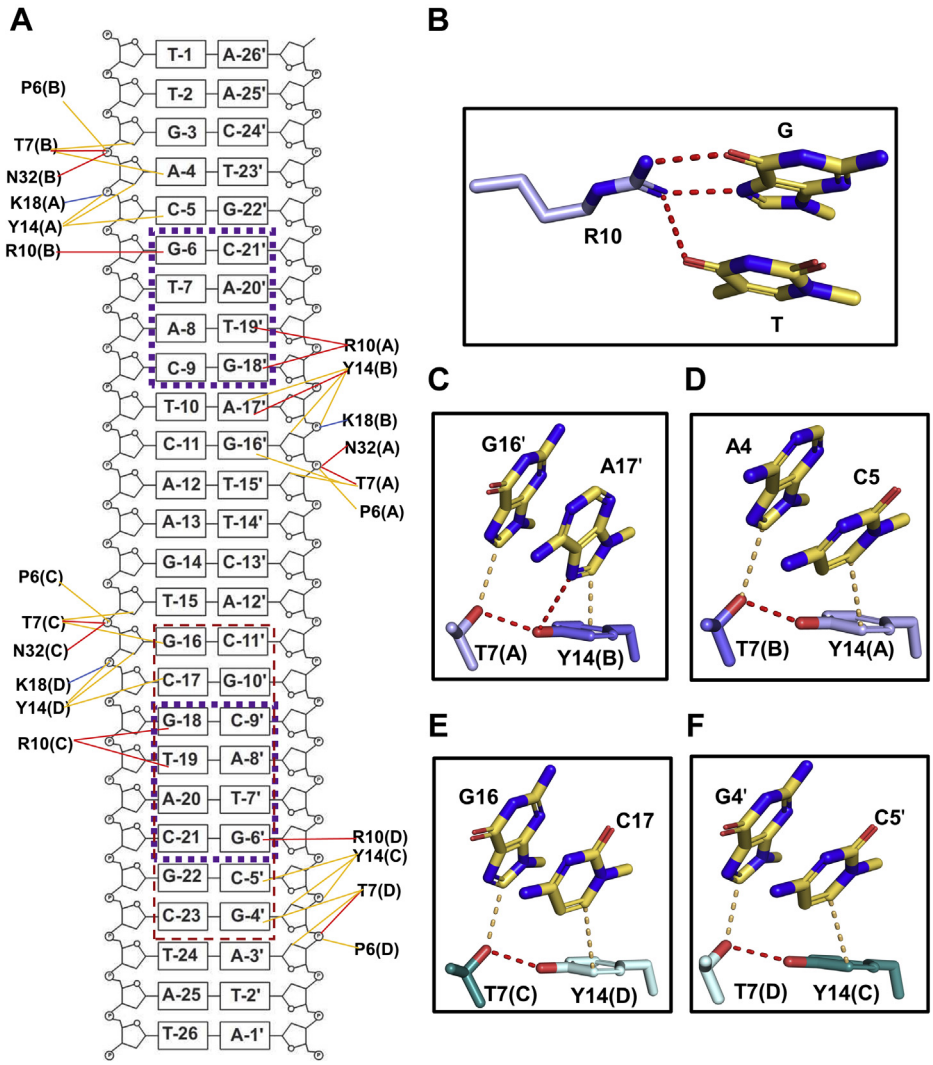

Figure 7. DNA recognition and binding pattern. *A*, schematic overview of the interactions between heterohexamer and DNA. *Red* and *yellow solid lines* depict hydrogen bond and van der Waals interactions, respectively. *Purple boxes* present the core GTAC and short palindromic sequence. *Red box* reflects the longer palindromic sequence. *B–F*, base-specific interactions of Sa_2YefM with promoter DNA. The hydrogen bonds and van der Waals interactions are presented as *red* and *yellow dashed lines*, respectively. The chain number of Sa_2YefM is presented in *parentheses*.

Tyr^{14}(A)/Tyr^{14}(B)/Tyr^{14}(C)/Tyr^{14}(D) lies perpendicular and forms VDW contacts with $C_5/A_{17'}/G_{5'}/C_{17}$ (Fig. 7, *C–F*). In addition, the terminal Oη group of Tyr^{14}(B) also donates hydrogen bond to the N7 atoms of $A_{17'}$. Moreover, the terminal Oγ group of Thr^7(A)/Thr^7(B)/Thr^7(C)/Thr^7(D) forms VDW contacts with the purine rings of $G_{16'}/A_4/G_{16}/G_{4'}$. Besides interacting with the bases, the side-chain hydroxyl group of Thr^7(A)/Thr^7(B)/Thr^7(C)/Thr^7(D) also forms hydrogen bond with the side-chain hydroxyl group of Tyr^{14}(B)/Tyr^{14}(A)/Tyr^{14}(D)/Tyr^{14}(C), respectively. Compared with the apoheterohexamer, hydroxyl groups of Thr^7 and Tyr^{14} in DNA-bound heterohexamer lie in close proximity (Fig. S7). Hydrogen bond of these two residues could fix orientation of the aromatic ring of Tyr^{14}, and the side chains of these residues could mediate VDW contacts with the nucleotides outside GTAC quadruplet. Hence, the VDW interaction and hydrogen bonds between residue (Thr^7) of one Sa_2YefM molecule of homodimer and residue (Tyr^{14}) of another SaYefM molecule of homodimer are mutually reinforcing interactions. Consistently, multiple-base pair substitutions (T_4: $A_{23'}$, T_5: $A_{22'}$, A_{10}: $T_{17'}$, A_{11}: $T_{16'}$, T_{16}: $A_{11'}$, T_{17}: $A_{10'}$, A_{22}: $T_{5'}$, and A_{23}: $T_{4'}$) of 26 bp probe demonstrated complete loss of binding affinity of heterohexamer against the mutated flanking sequence prompter (Fig. S6*B*), emphasizing the importance and specificity of the recognition of nucleotides outside the GTAC quadruplet by Sa_2YefM.

In addition to the base-specific interactions, Sa_2YefM also contributes in the extensive contacts with the phosphate backbone of promoter DNA as shown in Figure 7*A*. For instance, residues (Thr^7 and Asn^{32}) participated in hydrogen bond, whereas residues (Pro^6, Thr^7, and Tyr^{14}) are involved in the VDW contacts with the phosphate backbone of DNA. Besides, Lys^{18} of Sa_2YefM molecule could contact the phosphate backbone *via* the electrostatic interaction.

Comparison of recognition pattern of YefM and DNA of two YoeB–YefM paralogs revealed that the recognition of the core sequence "GTAC" is conserved, but the recognition pattern of flanking sequence for both paralogs is extremely

different. Sa_2YefM could recognize the bases "G" and "C" in the flanking sequence by residues Thr^7 and Tyr^{14}, whereas Sa_1YefM could specifically recognize the nucleotide "T" in the flanking sequence by residues Tyr^6 and Ser^7 (Fig. S8). Taken together, we concluded that the unique recognition of various flanking sequences could explain why two YefM–YoeB paralogs are transcriptionally autoregulated by their own cognate antitoxin.

Discussion

TA systems are ubiquitous genetic module found in varieties of bacteria and archea that could participate in various physiological processes, such as phage abortive infections, metabolism, cell growth, and viability during stress conditions (29). Type II TA systems are the most abundant genetic modules in bacterial species, in which both toxin and antitoxin form tight noncovalent complex. Many independent type II TA families, such as *ccdAB* (15), *relBE* (14), *VapBC* (30), and *phd–doc* (16), exhibit diverse oligomeric states. Previous research demonstrated that certain bacterial species possess multiple TA paralogous copies encoded by single chromosome. Each paralog could form independent functional unit. Fiebig *et al.* (31) reported that transcription of paralogous TA systems is differentially regulated under distinct environmental conditions. In *S. aureus*, two independent YefM–YoeB paralogous copies are present in the same strain (26). Our previous study demonstrated that Sa_1YoeB–Sa_1YefM exhibits two different oligomeric states (heterohexamer and heterotetramer), followed by the crystal structures of heterotetramer and heterohexamer–DNA (28). However, there is still lack of information about the apoheterohexamer structure. Consistent with our previous work (28), we obtained two different oligomeric states of Sa_2YefM–Sa_2YoeB paralog and solved the crystal structures of heterohexamer and heterotetramer in *apo*-form. Comparison of Sa_2YefM molecules within two different complexes demonstrated the mechanistic conformational changes in the C terminus and central helices of Sa_2YefM to stabilize the diverse oligomeric complexes. Previous research demonstrated that the free C-terminal intrinsic disorder region of *Ec*YefM within heterotrimer could not accommodate another *Ec*YoeB molecule, resulting in the collision of H4 helix of *Ec*YefM (22). Based on our resolved crystal structures, we speculated that the free C-terminal intrinsic disorder region of the *Ec*YefM within the heterotrimer could accommodate an additional *Ec*YoeB molecule by decreasing the angle between the central helices of the *Ec*YefM homodimer to prevent the collision of H4 helix in EcYefM molecule and ensure the stability of the *Ec*YefM–*Ec*YoeB heterotetramer.

Bacterial TA operons could be regulated by different molar ratios of antitoxin to toxin under different growth conditions. Imbalance in the molar ratio of both components might result in the cell cycle arrest or even cell death (32). Our previous study proposed the molecular mechanism for conditional cooperativity of the Sa_1YefM–Sa_1YoeB TA system (28). The transcriptional autoregulation of the Sa_2YefM–Sa_2YoeB paralogous copy is in agreement with the proposed molecular mechanism for Sa_1YefM–Sa_1YoeB module. Under normal growth conditions, Sa_2YefM antitoxin is expressed in higher concentration as compared with Sa_2YoeB toxin, which results in the formation of stable Sa_2YoeB_2–Sa_2YefM_4 heterohexamer. Similar to the Sa_1YefM–Sa_1YoeB TA system, the paralogous Sa_2YefM–Sa_2YoeB heterohexamer could also exhibit higher DNA-binding affinity. Comparative structural analysis of apo and DNA bound-heterohexamer demonstrated that the unique interaction of the heterohexamer with the promoter DNA induces the local region of the two SaYefM–SaYoeB heterotrimers to converge and bend the promoter DNA (Fig. S7*A*). The relative positions of N-terminal α helices (H1 and H2) of both Sa_2YefM homodimers inserted into the major groove are deflected by about 2.8 Å. These unique interactions result in stable Sa_2YoeB_2–Sa_2YefM_4–DNA ternary complex and eventually transcriptional repression. During stress conditions, accumulation of Sa_2YoeB increases the molar ratio of toxin to antitoxin, resulting in the formation of Sa_2YoeB_2–Sa_2YefM_2 heterotetramer. The simultaneous binding of two heterotetramers to the adjacent sites of the single promoter would sterically clash with each other, resulting in the release of heterotetramer and subsequently open the way for transcription. Collectively, these results demonstrated that both paralogous copies adopt similar mechanisms for their own transcriptional autoregulation.

Previous studies demonstrated that TA paralogs, including YefM–YoeB (*S. aureus* (26) and *Staphylococcus equorum* (33)), VapBC (*M. tuberculosis* (31)), paaR–paaA–pArE (*Escherichia coli* (34)), TacAT (*Salmonella typhimurium* (35)), and RelE/ParE (*Caulobacter crescentus* (31) and *Mycobacterium opportunistum* (36)), from the same bacterial chromosome are structurally insulated from the crossoperon interaction, suggesting independent function of each paralogous copy. However, there is still lack of information about the in-depth structural details of paralogous TA modules to investigate the molecular diversity in each paralogs. Grabe *et al.* (35) reported the crystal structures of three paralogous TacAT TA systems of *Salmonella* spp. to investigate the structural basis of the neutralizing interaction, specificity, and evolution of insulation across the three paralogs. Our structural analysis reflected that molecular diversity in the two YefM–YoeB paralogs is partly associated with different interaction profiles of YefM and YoeB, which is mediated by the conformational changes and acting forces at the C-terminal region of the YefM antitoxin. More or less similar trend of unique interaction patterns was also found in other TA systems. For instance, the conformational flexibility of the C-terminal region of the antitoxins in TacAT (*S. typhimurium* (35)) and ParDE (*M. opportunistum* (36)) paralogous modules is the main detrimental factor for the specificity across the corresponding paralogous copies. Collectively, our results reflected that the interactions between YefM and YoeB are unique for each YefM–YoeB paralogous copy; hence, we concluded that YefM from one system cannot abolish toxicity of YoeB from another system.

In addition to the unique interaction profiles of YefM and YoeB, different recognition patterns of the promoter DNA by

heterohexamer could be also associated with the structural insulation of the two YefM–YoeB paralogs. For most type II antitoxins containing HTH motif (HipB, HigA, GraA, and MsqA), the second helix of the HTH motif "the reading head" specifically recognizes the target DNA and deeply inserts into the major groove, and the first helix stabilizes the structure of motif (12). Unlike other HTH-type antitoxins, our structures of *Sa*YefM–*Sa*YoeB–DNA ternary complexes indicated that specific recognition of *Sa*YefM to DNA depends on the first helix or both helices rather than the second helix alone. For instance, residue Arg^{10}(H1) in both Sa_2YefM and Sa_1YefM recognizes the core "GTAC" sequence, whereas residues Thr^7(H1) and Tyr^{14}(H2) in Sa_2YefM and Tyr^6(H1), Ser^7(H1), and Gln^{11}(H1) in Sa_1YefM specifically recognize the nucleotides outside the GTAC quadruplet. The interactions of Arg^{10} with GTAC quadruplet, mediated by the helix H1 of YefM, are conserved in both paralogs. However, the interactions of residues (Thr^7 and Tyr^{14}) with the nucleotides outside the GTAC quadruplet are unique for Sa_2YefM, which is mainly associated with helices H1 and H2, respectively. Binding of promoter DNA to Sa_2YefM molecule could trigger the formation of hydrogen bonds between Thr^7 of one Sa_2YefM molecule of homodimer and Tyr^{14} of other Sa_2YefM molecule of the corresponding homodimer, followed by further reinforcing the VDW interactions between the flanking core sequences (G and C) and residues (Thr^7 and Tyr^{14}) of Sa_2YefM molecules. However, these residues are replaced with Tyr^6 and Ser^7 in Sa_1YefM that could recognize the flanking nucleotides (A and T) in the corresponding promoter. Moreover, binding energetics of heterohexamer–DNA interaction for both paralogs are also significantly different. For instance, isothermal calorimetric thermograms for Sa_1YefM–Sa_1YoeB reflected endothermic reaction, whereas Sa_2YefM–Sa_2YoeB paralogous copy adopts exothermic reaction. Together, these in-depth structural analyses highlight the molecular diversity of YefM–YoeB paralogous copies and could explain why Sa_2YefM–Sa_2YoeB do not cross talk with its paralog, and both systems could just regulate their own transcription. These results will further open the way to analyze the detailed molecular evolution of structural insulation in other TA paralogs.

Recently, the emergence of multidrug-resistant bacteria has attracted much attention from researchers. Previous research documented that many type II TA systems are more often found in pathogenic bacteria such as *M. tuberculosis* (37), *S. pneumoniae* (38), and *S. aureus* (39), resulting severe infections in human (40). Bacterial TA systems influence environmental stress-induced biofilm formation involved in numerous chronic disorders and antibiotic resistance (37). Qi *et al.* (39) reported that YoeB contributes in suppressing bacterial growth and is involved in antibiotic susceptibility. Deletion of YoeB toxin could result in antibiotic resistance under biofilm growth conditions. In addition, loss of both paralogous YoeB copies (Sa_1YoeB and Sa_2YoeB) could decrease the bacterial burden in neutropenic mouse abscess model (39). In addition, Sa_2YefM–Sa_2YoeB module could bind the promoter of virulence genes (*hla* and *efb*) that negatively regulate the expression of virulence gene, thus affecting the pathogenicity of *S. aureus* (41). However, the core GTAC quadruplet and the corresponding flanking sequence were not found in the promoter DNA of the virulence genes. Hence, we speculated that the expression of virulence genes might be regulated by Sa_2YoeB–Sa_2YefM type II TA system in an unknown way. These negative regulations of the virulence genes might result in the bactericidal effect and multidrug resistance activities of the *S. aureus*. As there are no human homologs for the TA systems and no pre-existing resistance against the TA toxins, hence, bacterial TA systems could be promising antimicrobial targets. The interaction of microbial growth, biofilm formation, antibiotic killing, and development of resistance is complex. Multiresistant activities of the pathogens could be ceased by several TA-based antimicrobial strategies, including (i) direct and indirect activation of TA systems utilizing various novel high-affinity peptides and (ii) engineered TA toxin–intein for targeted killing of the pathogenic bacteria by repressing the antitoxin expression, as previously reported for ccdA–ccdB type II TA system (42). Based on these results, we speculated that Sa_2YefM–Sa_2YoeB could be possible promising drug target that will shed light to develop promising antimicrobial strategy for other type II TA systems.

Experimental procedures

Plasmid constructions

Genes encoding Sa_2YefM antitoxin (SAOUHSC_02757) and Sa_2YoeB toxin (SAOUHSC_02756) were amplified from the genomic DNA of *S. aureus* (NCTC8325 strain), followed by constructing pET28a-*Sa_2yefM* (N-terminal hexahistidine), pET28a-*Sa_2yoeB* (N-terminal hexahistidine), *and* pET22b-*Sa_2yefM* (no tag) vectors. Mutant vectors encoding Sa_2YefM (Asn23Ala/Asp45Ala/Ser48Ala) and Sa_2YoeB (Ser45Ala/Arg60Ala/His63Ala) were obtained by site-directed mutagenesis utilizing the native pET22b-*Sa_2yefM* and pET28a-*Sa_2yoeB* vectors as a template, respectively. All constructs were confirmed with DNA sequencing. The oligonucleotide sequences for the construction of plasmids are listed in Table S1.

Protein expression and purification

Plasmid pET28a-*Sa_2yefM* was transformed into *E. coli* BL21(DE3) competent cells to obtain the recombinant Sa_2YefM protein. Native vectors (pET28a-*Sa_2yoeB* and pET22b-*Sa_2yefM*) and mutants (pET28a-*$Sa_2yoeB^{Ser45Ala/Arg60Ala/His63Ala}$* and pET22b-*$Sa_2yefM^{Asn23Ala/Asp45Ala/Ser48Ala}$*) were cotransformed into *E. coli* BL21(DE3) to express Sa_2YoeB_2–Sa_2YefM_4 heterohexamer and Sa_2YoeB–Sa_2YefM_2 heterotrimer, respectively (Table S2).

The transformants were inoculated in LB medium at 37 °C until an absorbance reached ~0.6 at 600 nm and induced with 0.5 mM IPTG at 16 °C for 18 h. Cells were harvested by centrifugation at 8000 rpm for 10 min, resuspended in buffer A (50 mM Tris–HCl, pH 8.0, 500 mM NaCl), and lysed with an ultrasonicator (Qsonica). Following centrifugation (12,000 rpm for 30 min at 4 °C), the supernatant was purified with immobilized affinity chromatography (Ni^{2+}–NTA column; GE Healthcare), followed by SEC (Superdex 16/200; GE

Healthcare), previously equilibrated with buffer B (20 mM Tris–HCl, pH 8.0, 300 mM NaCl). The quality of the purified proteins was analyzed with SDS-PAGE.

To obtain Sa_2YoeB alone and Sa_2YoeB$_2$–Sa_2YefM$_2$ heterotetramer complex, denaturing and refolding method was utilized. Briefly, purified heterohexamer (Sa_2YoeB$_2$–Sa_2YefM$_4$) was denatured in buffer C (20 mM Tris–HCl, pH 8.0, 7 M guanidine hydrochloride), followed by purification with Ni^{2+}–NTA column. Denatured Sa_2YoeB protein was purified in buffer C supplemented with the increasing concentration of imidazole. The purified version of denatured protein samples, that is, Sa_2YoeB and Sa_2YoeB:Sa_2YefM (1.2:1) were refolded by gradual dilution against buffer D (20 mM Tris–HCl, pH 8.0, 500 mM NaCl, and 5% glycerol) at 16 °C. The refolded protein samples were further purified with Superdex 16/200 column (GE Healthcare), previously equilibrated with buffer B. Fractions were pooled onto the SDS-PAGE.

SEC–MALS

SEC–MALS was applied to estimate the molecular weight of the specimens in solution. Briefly, protein samples (2 mg/ml) were loaded onto the Superdex 200 Increase 10/300 GL column (GE Healthcare) utilizing an AKTA purifier system (GE Healthcare). The system was coupled with 8-angle MALS detector (DAWN HELEOS II; Wyatt Technology) and differential refractometer (Optilab T-rEX; Wyatt Technology). ASTRA software suite (version 7.0.1.24) was used to determine the average weight molar mass of the samples.

Crystallization

Sitting drop vapor diffusion method was utilized to obtain crystals by mixing 1 μl protein sample with an equal volume of crystallization reservoir solution. Heterohexamer crystals were grown in 0.1 M ammonium tartrate dibasic at pH 7.0 and 12% w/v polyethylene glycol 3350, whereas heterotetramer crystals were grown in drop containing 0.2 M succinic acid at pH 7.0 and 20% w/v polyethylene glycol 3350. To obtain the crystal of Sa_2YoeB–Sa_2YefM–DNA ternary complex, heterohexamer was incubated with 26 bp promoter dsDNA (Table S1) at the molar ratio of 1:1.2 for 30 min, followed by mixing equal volume of protein–DNA complex with the reservoir solution. Crystal for heterohexamer–DNA was obtained in condition (0.02 M magnesium chloride hexahydrate, 0.05 M sodium cacodylate trihydrate at pH 7.0, 15% v/v 2-propanol, 0.001 M hexamine cobalt (III) chloride, and 0.001 M spermine).

Data collection and structure determination

Before flash-cooling in liquid nitrogen, all crystals were cryoprotected in the reservoir solution supplemented with 25% (v/v) glycerol. The diffraction datasets were collected on the beam lines BL17U1, BL18U1, and BL19U1 at the Shanghai Synchrotron Radiation Facility. All collected data were indexed, integrated, and scaled with HKL2000 software package (43).

Initial phases of the three structures were determined by molecular replacement method utilizing the Phenix.phaser (44). The initial structure of heterohexamer (Sa_2YoeB$_2$–Sa_2YefM$_4$) was resolved with the corresponding YoeB$^{Glu29–Tyr84}$–YefM$^{Met10–Leu64}$ from *E. coli* (Protein Data Bank accession code: 2A6Q) as a search model (22). Initial structures of the heterotetramer (Sa_2YoeB$_2$–Sa_2YefM$_2$) and heterohexamer–DNA (Sa_2YoeB$_2$–Sa_2YefM$_4$–DNA) were determined with partly resolved (Sa_2YoeB$^{Met1–Asp88}$–Sa_2YefM$^{Met1–Leu85}$) and whole Sa_2YoeB$_2$–Sa_2YefM$_4$ heterohexamer structures as search models, respectively. All structures were alternatively refined with Phenix (44, 45) for restrained refinement and Coot (46, 47) for manual modulation. Final structural models were prepared with PyMOL software suite. Summary of data collection and final refinement statistics are illustrated in Table S3.

EMSA

To validate the protein–DNA interactions, EMSAs were performed utilizing Chemiluminescent EMSA Kit (Beyotime Biotechnology), as per the manufacturer's instruction. The 26 bp dsDNA fragments corresponding the promoter sequence of *Sa2yefM–Sa2yoeB* operon were created by annealing two complementary oligonucleotides labeled with biotin at the 5′ end of the forward strand (Table S1). The biotin-labeled dsDNA fragment (2 nM) was incubated with protein (0–600 nM) in buffer B at room temperature for 20 min. Samples were subsequently loaded onto 6.5% native-PAGE at 80 V for 80 min, followed by transfer of biotin-labeled DNA to nylon membrane and subsequently UV-crosslinked at 302 nm for 15 min. The biotin-labeled DNA was detected *via* chemiluminescence, followed by obtaining the images with ImageQuant LAS 4000 mini (GE Healthcare).

ITC

To quantify the interaction of duplex DNA with the protein samples, ITC assays were performed utilizing Microcal PEAQ-ITC instrument (MicroCal, Inc) at 25 °C. The duplex DNA was created by annealing two complementary oligonucleotides in buffer B (Table S1). Duplex DNA (250–400 μM) was titrated against the protein sample (25–40 μM). Thermodynamic data were analyzed with a single-site binding model utilizing ITC data analysis module provided with the MicroCal PEAQ-ITC.

Data availability

The atomic coordinates have been deposited in the Protein Data Bank under the accession codes: 7V5Y for heterohexamer (Sa_2YoeB$_2$–Sa_2YefM$_4$); 7V5Z for heterotetramer (Sa_2YoeB$_2$–Sa_2YefM$_2$); and 7V6W for heterohexamer–DNA (Sa_2YoeB$_2$–Sa_2YefM$_4$–DNA).

Supporting information—This article contains supporting information.

Acknowledgments—We thank the staff at beamline BL17U1, BL18U1, and BL19U1 of the Shanghai Synchrotron Radiation Facility for help with data collection.

Author contributions—L. X. and M. H. K. conceptualization; L. X. and M. H. K. methodology; L. X. and M. H. K. software; J. Y. validation; L. X. and M. H. K. formal analysis; L. X. and M. H. K. data curation; L. X. and M. H. K. writing–original draft; J. Y. writing–reviewing & editing; Z. Z. and L. N. supervision.

Funding and additional information—This work was supported by the National Natural Science Foundation of China (U1632124 to L. N., 31270770 to Z. Z., and 31621002 to L. N.) and the Ministry of Science and Technology of China (2017YFA0503600 to L. N. and 2017YFA0504903 to L. N.). This work was also supported in part by the Hefei National Science Center Pilot Project Funds.

Conflict of interest—The authors declare that they have no conflicts of interest with the contents of this article.

Abbreviations—The abbreviations used are: HTH, helix–turn–helix; ITC, isothermal titration calorimetry; SEC–MALS, size-exclusion chromatography coupled with multilight angle scattering; TA, toxin–antitoxin; VDW, van der Waals.

References

1. Gerdes, K., Rasmussen, P. B., and Molin, S. (1986) Unique type of plasmid maintenance function: Postsegregational killing of plasmid-free cells. *Proc. Natl. Acad. Sci. U. S. A.* **83**, 3116–3120
2. Gerdes, K., Christensen, S. K., and Løbner-Olesen, A. (2005) Prokaryotic toxin-antitoxin stress response loci. *Nat. Rev. Microbiol.* **3**, 371–382
3. Lehnherr, H., Maguin, E., Jafri, S., and Yarmolinsky, M. B. (1993) Plasmid addiction genes of bacteriophage P1: Doc, which causes cell death on curing of prophage, and phd, which prevents host death when prophage is retained. *J. Mol. Biol.* **233**, 414–428
4. Lobato-Márquez, D., Díaz-Orejas, R., and García-Del Portillo, F. (2016) Toxin-antitoxins and bacterial virulence. *FEMS Microbiol. Rev.* **40**, 592–609
5. Page, R., and Peti, W. (2016) Toxin-antitoxin systems in bacterial growth arrest and persistence. *Nat. Chem. Biol.* **12**, 208–214
6. Paul, P., Sahu, B. R., and Suar, M. (2019) Plausible role of bacterial toxin-antitoxin system in persister cell formation and elimination. *Mol. Oral Microbiol.* **34**, 97–107
7. Bertram, R., and Schuster, C. F. (2014) Post-transcriptional regulation of gene expression in bacterial pathogens by toxin-antitoxin systems. *Front. Cell. Infect. Microbiol.* **4**, 6
8. Neubauer, C., Gao, Y. G., Andersen, K. R., Dunham, C. M., Kelley, A. C., Hentschel, J., Gerdes, K., Ramakrishnan, V., and Brodersen, D. E. (2009) The structural basis for mRNA recognition and cleavage by the ribosome-dependent endonuclease RelE. *Cell* **139**, 1084–1095
9. Pavelich, I. J., Maehigashi, T., Hoffer, E. D., Ruangprasert, A., Miles, S. J., and Dunham, C. M. (2019) Monomeric YoeB toxin retains RNase activity but adopts an obligate dimeric form for thermal stability. *Nucleic Acids Res.* **47**, 10400–10413
10. Liang, Y., Gao, Z., Wang, F., Zhang, Y., Dong, Y., and Liu, Q. (2014) Structural and functional characterization of Escherichia coli toxin-antitoxin complex DinJ-YafQ. *J. Biol. Chem.* **289**, 21191–21202
11. LeRoux, M., Culviner, P. H., Liu, Y. J., Littlehale, M. L., and Laub, M. T. (2020) Stress can induce transcription of toxin-antitoxin systems without activating toxin. *Mol. Cell* **79**, 280–292.e8
12. Chan, W. T., Espinosa, M., and Yeo, C. C. (2016) Keeping the wolves at bay: Antitoxins of prokaryotic type II toxin-antitoxin systems. *Front. Mol. Biosci.* **3**, 9
13. Harms, A., Brodersen, D. E., Mitarai, N., and Gerdes, K. (2018) Toxins, targets, and triggers: An overview of toxin-antitoxin biology. *Mol. Cell* **70**, 768–784
14. Bøggild, A., Sofos, N., Andersen, K. R., Feddersen, A., Easter, A. D., Passmore, L. A., and Brodersen, D. E. (2012) The crystal structure of the intact E. coli RelBE toxin-antitoxin complex provides the structural basis for conditional cooperativity. *Structure* **20**, 1641–1648
15. De Jonge, N., Garcia-Pino, A., Buts, L., Haesaerts, S., Charlier, D., Zangger, K., Wyns, L., De Greve, H., and Loris, R. (2009) Rejuvenation of CcdB-poisoned gyrase by an intrinsically disordered protein domain. *Mol. Cell* **35**, 154–163
16. Garcia-Pino, A., Balasubramanian, S., Wyns, L., Gazit, E., De Greve, H., Magnuson, R. D., Charlier, D., van Nuland, N. A., and Loris, R. (2010) Allostery and intrinsic disorder mediate transcription regulation by conditional cooperativity. *Cell* **142**, 101–111
17. Loris, R., and Garcia-Pino, A. (2014) Disorder- and dynamics-based regulatory mechanisms in toxin-antitoxin modules. *Chem. Rev.* **114**, 6933–6947
18. Chan, W. T., Moreno-Córdoba, I., Yeo, C. C., and Espinosa, M. (2012) Toxin-antitoxin genes of the Gram-positive pathogen Streptococcus pneumoniae: So few and yet so many. *Microbiol. Mol. Biol. Rev.* **76**, 773–791
19. Kumar, P., Issac, B., Dodson, E. J., Turkenburg, J. P., and Mande, S. C. (2008) Crystal structure of Mycobacterium tuberculosis YefM antitoxin reveals that it is not an intrinsically unstructured protein. *J. Mol. Biol.* **383**, 482–493
20. Zheng, C., Xu, J., Ren, S., Li, J., Xia, M., Chen, H., and Bei, W. (2015) Identification and characterization of the chromosomal yefM-yoeB toxin-antitoxin system of Streptococcus suis. *Sci. Rep.* **5**, 13125
21. Yoshizumi, S., Zhang, Y., Yamaguchi, Y., Chen, L., Kreiswirth, B. N., and Inouye, M. (2009) Staphylococcus aureus YoeB homologues inhibit translation initiation. *J. Bacteriol.* **191**, 5868–5872
22. Kamada, K., and Hanaoka, F. (2005) Conformational change in the catalytic site of the ribonuclease YoeB toxin by YefM antitoxin. *Mol. Cell* **19**, 497–509
23. Christensen, S. K., Maenhaut-Michel, G., Mine, N., Gottesman, S., Gerdes, K., and Van Melderen, L. (2004) Overproduction of the Lon protease triggers inhibition of translation in Escherichia coli: Involvement of the yefM-yoeB toxin-antitoxin system. *Mol. Microbiol.* **51**, 1705–1717
24. Feng, S., Chen, Y., Kamada, K., Wang, H., Tang, K., Wang, M., and Gao, Y. G. (2013) YoeB-ribosome structure: A canonical RNase that requires the ribosome for its specific activity. *Nucleic Acids Res.* **41**, 9549–9556
25. Donegan, N. P., and Cheung, A. L. (2009) Regulation of the mazEF toxin-antitoxin module in Staphylococcus aureus and its impact on sigB expression. *J. Bacteriol.* **191**, 2795–2805
26. Schuster, C. F., and Bertram, R. (2016) Toxin-antitoxin systems of Staphylococcus aureus. *Toxins (Basel)* **8**, 140
27. Sierra, R., Viollier, P., and Renzoni, A. (2019) Linking toxin-antitoxin systems with phenotypes: A Staphylococcus aureus viewpoint. *Biochim. Biophys. Acta Gene Regul. Mech.* **1862**, 742–751
28. Xue, L., Yue, J., Ke, J., Khan, M. H., Wen, W., Sun, B., Zhu, Z., and Niu, L. (2020) Distinct oligomeric structures of the YoeB–YefM complex provide insights into the conditional cooperativity of type II toxin–antitoxin system. *Nucleic Acids Res.* **48**, 10527–10541
29. Zhang, S. P., Feng, H. Z., Wang, Q., Kempher, M. L., Quan, S. W., Tao, X., Niu, S., Wang, Y., Feng, H. Y., and He, Y. X. (2021) Bacterial type II toxin-antitoxin systems acting through post-translational modifications. *Comput. Struct. Biotechnol. J.* **19**, 86–93
30. Winther, K. S., and Gerdes, K. (2012) Regulation of enteric vapBC transcription: Induction by VapC toxin dimer-breaking. *Nucleic Acids Res.* **40**, 4347–4357
31. Fiebig, A., Castro Rojas, C. M., Siegal-Gaskins, D., and Crosson, S. (2010) Interaction specificity, toxicity and regulation of a paralogous set of ParE/RelE-family toxin-antitoxin systems. *Mol. Microbiol.* **77**, 236–251
32. Zander, I., Shmidov, E., Roth, S., Ben-David, Y., Shoval, I., Shoshani, S., Danielli, A., and Banin, E. (2020) Characterization of PfiT/PfiA toxin-antitoxin system of Pseudomonas aeruginosa that affects cell elongation and prophage induction. *Environ. Microbiol.* **22**, 5048–5057
33. Nolle, N., Schuster, C. F., and Bertram, R. (2013) Two paralogous yefM-yoeB loci from Staphylococcus equorum encode functional toxin-antitoxin systems. *Microbiology (Reading)* **159**, 1575–1585

34. Hallez, R., Geeraerts, D., Sterckx, Y., Mine, N., Loris, R., and Van Melderen, L. (2010) New toxins homologous to ParE belonging to three-component toxin-antitoxin systems in Escherichia coli O157:H7. *Mol. Microbiol.* **76**, 719–732
35. Grabe, G. J., Giorgio, R. T., Hall, A. M. J., Morgan, R. M. L., Dubois, L., Sisley, T. A., Rycroft, J. A., Hare, S. A., and Helaine, S. (2021) Auxiliary interfaces support the evolution of specific toxin-antitoxin pairing. *Nat. Chem. Biol.* **17**, 1296–1304
36. Aakre, C. D., Herrou, J., Phung, T. N., Perchuk, B. S., Crosson, S., and Laub, M. T. (2015) Evolving new protein-protein interaction specificity through promiscuous intermediates. *Cell* **163**, 594–606
37. Kang, S. M., Kim, D. H., Jin, C., and Lee, B. J. (2018) A systematic overview of type II and III toxin-antitoxin systems with a focus on druggability. *Toxins (Basel)* **10**, 515
38. Chan, W. T., Nieto, C., Harikrishna, J. A., Khoo, S. K., Othman, R. Y., Espinosa, M., and Yeo, C. C. (2011) Genetic regulation of the yefM-yoeB toxin-antitoxin locus of Streptococcus pneumoniae. *J. Bacteriol.* **193**, 4612–4625
39. Qi, X., Brothers, K. M., Ma, D., Mandell, J. B., Donegan, N. P., Cheung, A. L., Richardson, A. R., and Urish, K. L. (2021) The *Staphylococcus aureus* toxin–antitoxin system YefM–YoeB is associated with antibiotic tolerance and extracellular dependent biofilm formation. *J. Bone Joint Infect.* **6**, 241–253
40. Xu, J., Zhang, N., Cao, M., Ren, S., Zeng, T., Qin, M., Zhao, X., Yuan, F., Chen, H., and Bei, W. (2018) Identification of three type II toxin-antitoxin systems in Streptococcus suis serotype 2. *Toxins (Basel)* **10**, 467
41. Wen, W., Liu, B., Xue, L., Zhu, Z., Niu, L., and Sun, B. (2018) Autoregulation and virulence control by the toxin-antitoxin system SavRS in Staphylococcus aureus. *Infect. Immun.* **86**, e00032-18
42. Rownicki, M., Lasek, R., Trylska, J., and Bartosik, D. (2020) Targeting type II toxin-antitoxin systems as antibacterial strategies. *Toxins (Basel)* **12**, 568
43. Otwinowski, Z., and Minor, W. (1997) Processing of X-ray diffraction data collected in oscillation mode. *Methods Enzymol.* **276**, 307–326
44. Adams, P. D., Afonine, P. V., Bunkóczi, G., Chen, V. B., Davis, I. W., Echols, N., Headd, J. J., Hung, L. W., Kapral, G. J., Grosse-Kunstleve, R. W., McCoy, A. J., Moriarty, N. W., Oeffner, R., Read, R. J., Richardson, D. C., *et al.* (2010) PHENIX: A comprehensive Python-based system for macromolecular structure solution. *Acta Crystallogr. D Biol. Crystallogr.* **66**, 213–221
45. Adams, P. D., Grosse-Kunstleve, R. W., Li, W. H., Ioerger, T. R., and Terwilliger, T. C. (2002) Phenix: building new software for automated crystallographic structure determination. *Acta Crystallogr. Sec. D Biolog. Crystallogr.* **58**, 1948–1954
46. Emsley, P., and Cowtan, K. (2004) Coot: Model-building tools for molecular graphics. *Acta Crystallogr. D Biol. Crystallogr.* **60**, 2126–2132
47. Emsley, P., B. Lohkamp, K., Scott, W., and Cowtan, K. (2010) Features and development of Coot. *Acta Crystallogr. D Biol. Crystallogr.* **66**, 486–501